# Direct-Estimation Algorithm for Mapping Daily Land-Surface Broadband Albedo From MODIS Data

Ying Qu, Qiang Liu, Shunlin Liang, *Fellow, IEEE*, Lizhao Wang, Nanfeng Liu, and Suhong Liu

*Abstract*—Land surface albedo is a critical parameter in surface-energy budget studies. Over the past several decades, many albedo products are generated from remote-sensing data sets. The Moderate Resolution Imaging Spectroradiometer (MODIS) bidirectional reflectance distribution function (BRDF)/Albedo algorithm is used to routinely produce eight day (16-day composite), 1-km resolution MODIS albedo products. When some natural processes or human activities occur, the land-surface broadband albedo can change rapidly, so it is necessary to enhance the temporal resolution of albedo product. We present a direct-estimation algorithm for mapping daily land-surface broadband albedo from MODIS data. The polarization and directionality of the Earth's reflectance-3/polarization and anisotropy of reflectances for atmospheric sciences coupled with observations from a Lidar BRDF database is employed as a training data set, and the 6S atmospheric radiative transfer code is used to simulate the top-of-atmosphere (TOA) reflectances. Then a relationship between TOA reflectances and land-surface broadband albedos is developed using an angular bin regression method. The robustness of this method for different angular bins, aerosol conditions, and land-cover types is analyzed. Simulation results show that the absolute error of this algorithm is ∼0.009 for vegetation, 0.012 for soil, and 0.030 for snow/ice. Validation of the direct-estimation algorithm against *in situ* measurement data shows that the proposed method is capable of characterizing the temporal variation of albedo, especially when the land-surface BRDF changes rapidly.

*Index Terms*—Angular bin regression, direct-estimation algorithm, land-surface broadband albedo, Moderate Resolution Imaging Spectroradiometer (MODIS), polarization and directionality of the Earth's reflectance (POLDER) bidirectional reflectance distribution function (BRDF) database.

## I. INTRODUCTION

LAND surface albedo, defined as the fraction of incident solar radiation (0.3–5.0 $\mu$m) reflected by land surfaces [1], [2], is one of the most important parameters in general circulation models, hydrology models, numerical weather models, and surface-radiation-budget studies.

There are several projects focused on monitoring the spatiotemporal variations of land-surface albedo at observation sites distributed throughout the world. However, it is not sufficient to use these data directly in climate models. Because different climate models compute albedo differently, their estimates can differ significantly [3]. Simultaneously, satellite observations can provide a global albedo product with higher spatial and temporal resolution, which is more suitable for global-change studies.

Over the past several decades, many albedo products with spatial resolutions of 500 m to 20 km and temporal frequencies ranging from daily to monthly are produced from different remote-sensing data sets, such as the Moderate Resolution Imaging Spectroradiometer (MODIS) [4]–[6], polarization and directionality of the Earth's reflectance (POLDER) [7]–[11], Medium Resolution Imaging Spectrometer (MERIS) [12], Clouds and the Earth's Radiant Energy System (CERES) [13], Meteosat Second Generation (MSG) [14], [15] and meteosat [16]–[20].

The MODIS bidirectional reflectance distribution function (BRDF)/Albedo algorithm [6] is routinely used for producing the MCD43 series of albedo products. The MODIS 1-km broadband albedo product is produced by inverting multidate, multiangular, cloud-free, atmospherically corrected surface reflectances acquired by the MODIS instrument onboard the Terra and Aqua satellites. In general, it is carried out in three steps: 1) atmospheric correction; 2) surface angular modeling; and 3) narrowband-to-broadband albedo conversions. Each step has an explicit physical foundation. However, the errors from each step may accumulate and affect the accuracy of the final albedo product. For example, the atmospheric correction of the MODIS top-of-atmosphere (TOA) reflectance depends

Y. Qu, L. Wang, and S. Liu are with the School of Geography, Beijing Normal University, Beijing 100875, China, and also with the State Key Laboratory of Remote Sensing Science, Jointly Sponsored by Beijing Normal University and Institute of Remote Sensing Applications of Chinese Academy of Sciences, Beijing 100875, China (e-mail: quying@mail.bnu.edu.cn; wlz1220@sina.com; liush@bnu.edu.cn).

Q. Liu is with the College of Global Change and Earth System Science, Beijing Normal University, Beijing 100875, China; Institute of Remote Sensing Applications, Chinese Academy of Sciences, Beijing 100875, China, and also with the State Key Laboratory of Remote Sensing Science, Jointly Sponsored by Beijing Normal University and Institute of Remote Sensing Applications of Chinese Academy of Sciences, Beijing 100875, China (email: liuqiang@irsa.ac.cn).

S. Liang is with the College of Global Change and Earth System Science, Beijing Normal University, Beijing 100875, China; Department of Geography, University of Maryland, College Park, Maryland, USA, and also with the State Key Laboratory of Remote Sensing Science, Jointly Sponsored by Beijing Normal University and Institute of Remote Sensing Applications of Chinese Academy of Sciences, Beijing 100875, China (e-mail: sliang@umd.edu).

N. Liu is with the Institute of Remote Sensing Applications, Chinese Academy of Sciences, Beijing, China, and also with the State Key Laboratory of Remote Sensing Science, Jointly Sponsored by Beijing Normal University and Institute of Remote Sensing Applications of Chinese Academy of Sciences, Beijing 100875, China (e-mail: liunanfengrs@163.com).

Color versions of one or more of the figures in this paper are available online at http://ieeexplore.ieee.org.

Digital Object Identifier 10.1109/TGRS.2013.2245670

This article has been accepted for inclusion in a future issue of this journal. Content is final as presented, with the exception of pagination.

2

IEEE TRANSACTIONS ON GEOSCIENCE AND REMOTE SENSING

on the performance of the aerosol retrieval algorithm. When the algorithm for estimating the aerosol optical depth (AOD) is not applicable (e.g., no "dark objects" can be found in the scene), the atmospheric-corrected reflectance product can be unreliable [21].

The temporal resolution of the MCD43B3 collection five products is eight days, and the temporal resolution of a newly proposed product called the "direct broadcast" albedo product [22] is daily. However, all of these products are based on a 16-day cycle's observed data. This observation strategy assumes that the land-surface reflectance signature does not change during the 16-day cycle, which is not always valid. For instance, when several natural processes (e.g., snowfall, snowmelt, precipitation, and vegetation growth) and human activities (e.g., clearing and planting forests, sowing and harvesting crops, burning rangeland) occur, the land surface albedo can change rapidly [23]. In other words, the algorithms based on multidate observations cannot capture phenomena with rapidly changing albedos.

The alternative is to develop an empirical relationship between the TOA reflectances and surface broadband albedos [24]–[26]. This method produces a daily albedo product using just one scene of MODIS data in each retrieval process, which is usually called the direct-estimation algorithm. Liang *et al.* [24] used the MODTRAN package to simulate TOA reflectances under the Lambertian assumption, and they obtained a relationship between MODIS TOA reflectances and broadband albedos by using a neural network method. Liang [25] used the projection pursuit regression method. However, these two studies did not consider the anisotropy of the land surface. Liang *et al.* [26] further improved it for estimating daily land surface albedo of the Greenland ice sheet from MODIS data. They used the discrete ordinates radiative transfer program for a multilayered plane-parallel medium to simulate TOA reflectances of snow/ice and then developed the relationship between bidirectional TOA reflectances and broadband albedos using an empirical training method; they divided the solar/view geometry space into angular bins and calculated the regression coefficients of each angular bin using a linear regression method.

Cui *et al.* [27] used the POLDER-2 BRDF database to develop a relationship between surface reflectances and broadband albedos using simple linear regression at different solar zenith angles (SZAs) and phase angles. This method can be considered an anisotropy-correction method, which is very accurate for snow/ice-free land surfaces under clear-sky conditions.

In this paper, we developed a new direct-estimation algorithm by employing the 6S (second simulation of a satellite signal in the solar spectrum) atmospheric radiative transfer code [28] to simulate the TOA directional reflectances, calculating the broadband albedos based on the POLDER BRDF data set, and then establishing a relationship between the TOA reflectances and surface broadband albedos using an angular bin regression method.

## II. METHODOLOGY

The direct-estimation algorithm is an empirical method of estimating broadband land surface albedo based on the BRDF database. To develop a statistical relationship between
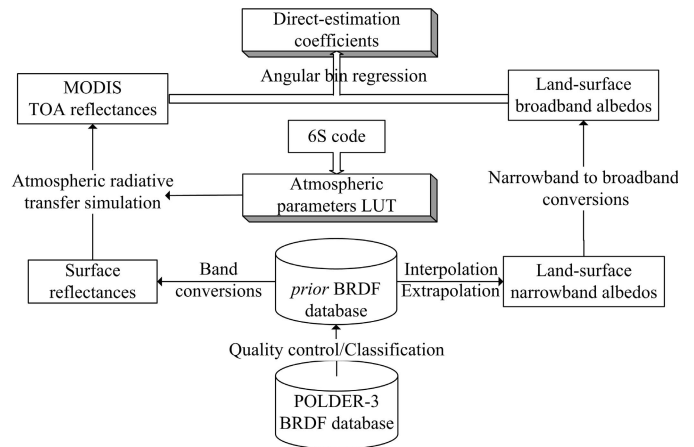


Fig. 1. Flow chart to derive the coefficients for the direct-estimation algorithm.

satellite-observed TOA directional reflectances and the land-surface broadband albedos, a training data set is needed. To this end, we initially constructed a surface BRDF database and then simulated the TOA directional reflectances with the atmospheric radiative transfer model. The broadband albedos are derived from narrowband albedos calculated by a revised linear kernel-driven model. Finally, a relationship between TOA directional reflectances and broadband albedos is developed using an angular bin regression method. The essential part of the algorithm is to derive the empirical regression coefficients for each of the angular bin, and then it is very simple to use these coefficients to estimate broadband albedo from MODIS observations. The flow chart for the regression coefficients is shown in Fig. 1.

In the following sections, we initially address the issue of building the training data set and the atmospheric radiative transfer model, and then provide a detailed description of the angular bin regression method.

### A. Training Data Set

*1) POLDER-3/Polarization and Anisotropy of Reflectances for Atmospheric Sciences Coupled With Observations From a Lidar BRDF Database:* In [25] and [29], the data sets of field or laboratory spectra are used to represent the reflectance properties of different types of land surfaces. However, the reflectance anisotropy of land-surface objects are not considered. The BRDF database is needed as *a prior* knowledge to compute the land-surface broadband albedos using the TOA directional reflectances observed by satellite sensors. Unfortunately, the ground-measured data are not suitable for direct comparison with satellite acquired data, as the scale of the ground-measured data is not compatible with the satellite data, and currently there are not enough ground-measured BRDF data sets to represent all the various land-cover types in a global scope. Therefore, the satellite directional observation data set is more suitable for training data in our paper. To the best of our knowledge, the POLDER BRDF database produced by POSTEL service center/MEDIAS-France is an ideal anisotropy reflectance database that meets our requirements.

The POLDER-3/polarization and anisotropy of reflectances for atmospheric sciences coupled with observations from a Lidar (PARASOL) BRDF database can be down-loaded from the internet: (URL: http://postel.mediasfrance.org/en/

This article has been accepted for inclusion in a future issue of this journal. Content is final as presented, with the exception of pagination.

QU *et al.*: DIRECT-ESTIMATION ALGORITHM FOR MAPPING DAILY LAND-SURFACE BROADBAND ALBEDO 3

BIOGEOPHYSICAL-PRODUCTS/BRDF). The POLDER-3 radiometer onboard the CNES/Parasol satellite provides multidirectional measurements of the Earth reflectances at six bands (the center wavelengths are 490, 565, 670, 765, 865, and 1020 nm). In each overpass of the satellite, the POLDER instrument acquires up to 16 reflectance measurements of land surfaces from different directions, with a maximum view zenith angle (VZA) of 70°. The directional reflectance is corrected for molecular and aerosols scattering, as well as atmospheric absorption [10], [30]. Each sample (pixel) of the BRDF database is an accumulation set of one-month atmospheric-corrected bidirectional reflectance factors (BRFs) from different satellite overpasses. For each sample, 80–500 angular samplings semihomogenously distributed in the viewing hemisphere can be obtained. The samples of POLDER-3/PARASOL BRDF database are selected through a series of selection procedures. These selection procedures are carried out in three steps: 1) the selection of thematically homogeneous pixels, according to the land-cover map [the land-cover classification scheme of the international geosphere-biosphere program (IGBP)] or GLC2000 (global land cover map for the year 2000); 2) a preselection procedure according to the quality of the inversion of the reflectance model against one month of data for removing the noisiest BRDFs and those with few observations; and 3) the final selection procedure that accounts for the quality of the reflectance model inversion over one single orbit.

There are two significant improvements in the most recent version of POLDER database (POLDER-3/PARASOL BRDF database): 1) POLDER-3 BRDF data are acquired over 12 months from November 2005 to October 2006 whereas POLDER-1 and 2 BRDF data are acquired over eight and seven months, respectively, and data from a full year provide a much better representation of the seasonal variations of land surface albedo, and 2) the POLDER-3 instrument is onboard the microsatellite PARASOL. The POLDER-3/PARASOL BRDF database contains 13 887 samples (pixels) that present different landscapes at different locations with a spatial resolution of 6 km. Each sample of the data set is composited using monthly observed data. The data set contains all types of IGBP classes, and it is distributed widely throughout the world.

*2) Interpolation and Extrapolation for the BRDF Database:* When the SZA is 60° or 20°, the observations are particularly rare, so the POLDER-3/PARASOL database need to be interpolated and extrapolated to build the complete training data set. The most acknowledged method of fitting and predicting BRDF is the linear kernel-driven model [31], [32], in which the BRF is expressed as follows:

$$R(\theta_s, \theta_v, \varphi; \lambda) = f_{\text{iso}}(\lambda) + f_{\text{vol}}(\lambda)k_{\text{vol}}(\theta_s, \theta_v, \varphi)$$
$$+ f_{\text{geo}}(\lambda)k_{\text{geo}}(\theta_s, \theta_v, \varphi) \quad (1)$$

where $\theta_s$ is SZA; $\theta_v$ is VZA; $\varphi$ is relative azimuth angle (RAA); $\lambda$ is the wavelength; and $k_{\text{vol}}$ and $k_{\text{geo}}$ are the volume scattering and geo-optical kernels, respectively; $f_{\text{iso}}$, $f_{\text{vol}}$, and $f_{\text{geo}}$ are the coefficients of isotropic, volume scattering, and geo-optical kernel, respectively.

The original linear kernel-driven model proposed by Wanner *et al.* [31] is especially suitable for accounting the backward-scattering effect of the directional reflectance from vegetation canopy. Because of the strong forward-scattering effects of directional reflectances of snow/ice in the polar area [33], a forward-scattering kernel is needed. After extensive comparisons of several different models, we revise the original linear kernel-driven model as follows:

$$R(\theta_s, \theta_v, \varphi; \lambda) = f_{\text{iso}}(\lambda) + f_{\text{vol}}(\lambda)k_{\text{vol}}(\theta_s, \theta_v, \varphi)$$
$$+ f_{\text{geo}}(\lambda)k_{\text{geo}}(\theta_s, \theta_v, \varphi) + f_{\text{fwd}}(\lambda)k_{\text{fwd}}(\theta_s, \theta_v, \varphi) \quad (2)$$

where $k_{\text{fwd}}(\theta_s, \theta_v, \varphi)$ and $f_{\text{fwd}}(\lambda)$ are the forward-scattering kernel and its coefficients, respectively. A revised Ross-Thick kernel that accounts for the hot-spot effect [11] is used as the volume scattering kernel, and the Li-Sparse-R kernel [34] is used as the geometry optical kernel. The forward-scattering kernel is added to describe the forward-scattering effects for snow surfaces and is derived by simplifying the Rahman–Pinty–Verstraete model [35] and fixing the parameters to typical values

$$k_{\text{fwd}}(\theta_s, \theta_v, \varphi) = \frac{\cos^{k-1}\theta_s \cos^{k-1}\theta_v}{(\cos\theta_s + \cos\theta_v)^{1-k}}$$
$$\cdot \frac{1-g^2}{(1+g^2-2g\cos(\pi-\xi))^{3/2}} - \frac{1+g}{2^{1-k}(1-g)^2} \quad (3)$$

where $g = 0.0667$ and $k = 0.846$. $\cos\xi = \cos\theta_s \cos\theta_v + \sin\theta_s \sin\theta_v \cos\phi$.

The BRF measurements are used to retrieve the kernel parameters of (2), which are then applied to interpolate and extrapolate the BRDF data to an arbitrary incident/view angle. The uncertainties of the interpolations and extrapolations increase as the solar/VZA increases, and the maximum root-mean-square error (RMSE) is ~0.005. Although the quality control of the POLDER-3 BRDF database is very efficient, we found that the consistency of several BRDF samples is not good because of the BRDF characteristic changes during the one-month collection period (e.g., snow fall and snow melt processes, soil moisture changes). To screen out the data sets that are not suitable for our study, the following criteria are adopted:

1) $\gamma_{490} < 0.01$ and $\gamma_{490}/\mu_{490} < 0.3$;
2) $\gamma_{\text{total}} < 0.1$ and $\gamma_{\text{total}}/\mu_{total} < 0.2$;
3) the number of orbits is $>4$, and the total observation number is $>80$.

Here, $\gamma_{490}$ is the RMSE of the fitting result for POLDER band one, which is centered at 490 nm; $\gamma_{\text{total}}$ is the sum RMSE of the fitting result for six bands (490, 565, 670, 765, 865, and 1020 nm); $\mu_{490}$ is the mean value of the reflectance at 490 nm; and $\mu_{\text{total}}$ is the mean value across all the six bands (490, 565, 670, 765, 865, and 1020 nm). When the data is contaminated by clouds, or there is drastic change in surface properties (such as before and after snow), the value of $\gamma_{\text{total}}$ and $\gamma_{490}$ is usually much higher than usual. The third criterion screens out data sets with insufficient sample numbers. All of these thresholds are empirical coefficients that are determined by visual interpretation. After this process, the data of 4863 pixels are screened out, and the remaining 9024 pixels are employed in the following steps.

*3) Band Conversions From POLDER to MODIS:* The directional reflectances at MODIS bands are needed in this paper. Because reflectances at different wavelengths are highly correlated [36], the band conversions from POLDER to MODIS

This article has been accepted for inclusion in a future issue of this journal. Content is final as presented, with the exception of pagination.

4

IEEE TRANSACTIONS ON GEOSCIENCE AND REMOTE SENSING

TABLE I
BAND CONVERSION COEFFICIENTS (FROM POLDER TO MODIS)

| Band Name | $c_1$ POLDER- (490 nm) | $c_2$ POLDER- (565 nm) | $c_3$ POLDER- (670 nm) | $c_4$ POLDER- (765 nm) | $c_5$ POLDER- (865 nm) | $c_6$ POLDER- (1020 nm) | $c_0$ (offset) | RMSE |
|---|---|---|---|---|---|---|---|---|
| MODIS (648 nm) | 0.025804 | 0.310757 | 0.686464 | −0.039359 | −0.013607 | 0.03182 | 0.004839 | 0.003081 |
| MODIS (859 nm) | 0.025002 | −0.027624 | −0.011339 | 0.26367 | 0.701168 | 0.05768 | 0.000611 | 0.00339 |
| MODIS (466 nm) | 0.91419 | 0.141745 | −0.060689 | 0.013902 | 0.010337 | −0.022371 | −0.007441 | 0.004179 |
| MODIS (554 nm) | 0.205108 | 0.610729 | 0.125942 | 0.11475 | −0.01769 | −0.046839 | −0.001009 | 0.004307 |
| MODIS (1244 nm) | −0.372893 | 0.016735 | 0.406773 | −0.205036 | −0.450877 | 1.432253 | 0.023339 | 0.021808 |
| MODIS (1631 nm) | −1.062408 | −0.380808 | 1.514777 | −0.370976 | −0.53941 | 1.169188 | 0.073113 | 0.043379 |
| MODIS (2119 nm) | −1.177391 | −0.444721 | 1.798923 | −0.303519 | −0.517468 | 0.818367 | 0.072311 | 0.048518 |

can be achieved through a statistical approach

$$\rho_{\text{MODIS}}(\lambda_i) = c_0 + \sum_{j=1}^{n} c_j \rho_{\text{POLDER}}(\lambda_j) \qquad (4)$$

where $\rho_{\text{MODIS}}(\lambda_i)$ are the MODIS reflectances at $\lambda_i$, $\rho_{\text{POLDER}}(\lambda_j)$ are the POLDER-3 reflectances at $\lambda_j$, $c_0$ is the intersection term, and $c_j$ are the conversions coefficients. The intersection terms and coefficients are derived by linear regression using the following ground-measured spectral data sets: spectral reflectance data presented in quantitative remote sensing of land surfaces [37] (119 samples), the spectral library of Beijing Normal University (URL: http://spl.bnu.edu.cn, 224 samples), the database of watershed allied telemetry experimental research (WATER) Experiment (URL: http://westdc.westgis.ac.cn/water/zy, 103 samples), and the snow reflectance data set measured in Greenland (47 samples). The coefficients and RMSE values of the regression function are shown in Table I. The RMSE values of the visible-infrared bands of MODIS (648, 859, 466, and 554 nm) are smaller than those of the short-wave infrared bands of MODIS (1244, 1631, and 2119 nm), because the POLDER instrument does not have the shortwave infrared bands. Thus, the bands at 1244, 1631, and 2119 nm are not used in our regression analysis approach because the band-conversion errors for these bands are large.

*4) Method for Deriving Broadband Albedos:* The instantaneous albedo (blue-sky albedo) can be expressed in the form of [5] and [38]

$$\alpha(\theta_s, \lambda) = \alpha_{bs}(\theta_s, \lambda)(1 - D(\theta_s, \tau(\lambda))) + \alpha_{ws}(\lambda)D(\theta_s, \tau(\lambda)) \qquad (5)$$

where $\alpha(\theta_s)$ is the actual albedo at wavelength $\lambda$, $D(\theta_s, \tau(\lambda))$ is the fraction of diffuse skylight when the SZA is $\theta_s$, $\tau(\lambda)$ is the AOD at wavelength $\lambda$, $\alpha_{bs}$ is the black-sky albedo (directional-hemispheric albedo), and $\alpha_{ws}$ is the white-sky albedo (bihemispheric albedo). The fraction of diffuse skylight changes with SZA, AOD, bands, and aerosol model types. It can be calculated by a predetermined look up table (LUT) based on 6S atmospheric radiative transfer code.

If the BRDF is retrieved by the linear kernel-driven model, the black-sky and white-sky albedos can be calculated as

follows [5]:

$$\alpha_{bs}(\theta_s, \lambda) = \sum_k f_k(\lambda)h_k(\theta_s) \qquad (6)$$

$$\alpha_{ws}(\lambda) = \sum_k f_k(\lambda)H_k \qquad (7)$$

where $h_k(\theta_s)$ is the integral of kernels $k$ over view hemisphere when the SZA is $\theta_s$, and $H_k$ is the integral of $h_k(\theta_s)$ over incidence hemisphere. $f_k$ are the coefficients of linear kernel-driven model kernels $k$.

The narrowband-to-broadband conversions can be expressed by [29]

$$\alpha = c_0 + \sum_{i=1}^{n} c_i \alpha(\lambda_i) \qquad (8)$$

where $\alpha$ is the broadband albedo, $\alpha(\lambda)$ is the spectral (narrowband) albedo, and $c_i$ ($i = 0, 1, \ldots, n$, where $n$ is the number of bands) are the coefficients for band conversions. The conversion coefficients (Table II) for narrowband-to-broadband conversions are derived in several previous studies [29], [39].

### B. Atmospheric Radiative Transfer Simulation

In this paper, the 6S atmospheric radiative transfer code is used to simulate the TOA directional reflectances. To avoid extremely large computations, we did not use the 6S module directly. Instead, a fast and accurate approximation method proposed by Qin [40] is chosen to simulate the TOA directional reflectances. This method is especially suitable for simulating the atmospheric effects over nonlambertian land surfaces. To eliminate the effects of water vapor absorption, the original equation is reformulated based on the 6S atmospheric radiative transfer code [28] as in (9), shown at the bottom of this page, where the matrices $T(\theta_s)$, $R(\theta_s, \theta_v, \varphi)$, and $T(\theta_v)$ are defined as

$$T(\theta_s) = [t_{dd}(\theta_s)\ t_{dh}(\theta_s)], \quad T(\theta_v) = \begin{bmatrix} t_{dd}(\theta_v) \\ t_{hd}(\theta_v) \end{bmatrix}$$

$$R(i, v) = \begin{bmatrix} r_{dd}(\theta_s, \theta_v, \varphi)\ r_{dh}(\theta_s, \varphi_s) \\ r_{hd}(\theta_v, \varphi_v)\ \quad r_{hh} \end{bmatrix}.$$

Subscripts $s$ and $v$ stand for solar illumination and viewing direction, respectively; $\theta_s$, $\theta_v$, $\varphi_s$, $\varphi_v$, and $\varphi$ are

$$\rho^{\text{TOA}}(\theta_s, \theta_v, \varphi) = t_{\text{H}_2\text{O}} \times \left[ \rho_0(\theta_s, \theta_v, \varphi) + \frac{T(\theta_s) \cdot R(\theta_s, \theta_v, \varphi) \cdot T(\theta_v) - t_{dd}(\theta_s) \cdot t_{dd}(\theta_v) \cdot |R(\theta_s, \theta_v, \varphi)| \cdot \overline{\rho}}{1 - r_{hh}\overline{\rho}} \right] \qquad (9)$$

This article has been accepted for inclusion in a future issue of this journal. Content is final as presented, with the exception of pagination.

QU *et al.*: DIRECT-ESTIMATION ALGORITHM FOR MAPPING DAILY LAND-SURFACE BROADBAND ALBEDO

5

TABLE II

NARROWBAND-TO-BROADBAND CONVERSION COEFFICIENTS

| MODIS Bands ($\mu$m) | c0 (offset) | c1 (0.62–0.67) | c2 (0.84–0.87) | c3 (0.46–0.48) | c4 (0.54–0.56) | c5 (1.23–1.25) | c6 (1.63–1.65) | c7 (2.11–2.15) |
|---|---|---|---|---|---|---|---|---|
| Snow/ice free | −0.0015 | 0.1600 | 0.2910 | 0.2430 | 0.1160 | 0.1120 | 0.0000 | 0.0810 |
| Snow/ice | −0.0093 | 0.1574 | 0.2789 | 0.3829 | 0.0000 | 0.1131 | 0.0000 | 0.0694 |

TABLE III

INPUT SETTINGS FOR PARAMETERS OF 6S ATMOSPHERIC RADIATIVE TRANSFER CODE

| Parameters | Input Settings |
|---|---|
| Atmospheric type | Tropical, Midlatitude Summer, Midlatitude Winter, Subarctic Summer, Subarctic Winter, US62 |
| Aerosol type | Continental, Maritime, Urban, Desert, Biomass burning, Haze |
| AOD | 0.1, 0.2, 0.25, 0.3, 0.35, 0.4 |
| Target altitude | 0, 0.5, 1.0, 1.5, 2.0, 2.5, 3, 3.5 (km) |
| Solar zenith | 0, 4, 8, ..., 76, 80 (degree) |
| View zenith | 0, 4, 8, ..., 60, 64 (degree) |
| Relative azimuth | 0, 20, 40, ..., 160, 180 (degree) |

the SZA, VZA, solar azimuth angle, view azimuth angle, and RAA, respectively; and $t$ and $r$ represent transmittance and reflectance, respectively; $\rho^{\text{TOA}}(\theta_s, \theta_v, \varphi)$ is the TOA directional reflectance; $\rho_0(\theta_s, \theta_v, \varphi)$ is the path scattering reflectance of the atmosphere; $t_{\text{H}_2\text{O}}$ is the transmittance of the water vapor; $\overline{\rho}$ is the spherical albedo of the atmosphere. The subscripts $h$ and $d$ stand for hemispheric (diffuse) and directional (direct), respectively, and the four combinations of these two symbols $dd$, $dh$, $hd$, and $hh$ stand for bidirectional, directional-hemispheric, hemispheric-directional, and bihemisphere, respectively. Thus, $t_{dd}(\theta_s)$ and $t_{dd}(\theta_v)$ are the downward and upward bidirectional path transmittances, respectively; and $t_{dh}(\theta_s)$ and $t_{hd}(\theta_v)$ are the directional-to-hemispheric path transmittance and the hemispheric-to-directional transmittance, respectively. $r_{dd}(\theta_s, \theta_v, \varphi)$, $r_{dh}(\theta_s, \varphi_s)$, $r_{hd}(\theta_v, \varphi_v)$, and $r_{hh}$ are the surface bidirectional reflectance, directional-to-hemispheric reflectance, hemispheric-to-directional reflectance and bihemispheric reflectance (BHR), respectively. The values of $r_{dh}(\theta_s, \varphi_s)$, $r_{hd}(\theta_v, \varphi_v)$, and $r_{hh}$ are calculated using the POLDER-3/PARASOL BRDF database, and the values of $\rho_0(\theta_s, \theta_v, \varphi)$, $t_{dh}(\theta_s)$, $t_{hd}(\theta_v)$, $t_{dd}(\theta_s)$, $t_{dd}(\theta_v)$, $\overline{\rho}$, and $t_{\text{H}_2\text{O}}$ are acquired using a LUT produced by the 6S atmospheric radiative transfer code.

In this paper, the 6S radiative transfer code is selected as a tool for developing the LUT, which contains the atmospheric parameters used in (9). The LUT has seven dimensions: atmosphere type, aerosol type, AOD, target elevation, SZA, VZA, and RAA. The input parameters for the 6S code are set as follows (Table III): six atmosphere types (tropical, midlatitude summer, midlatitude winter, subarctic summer, subarctic winter, and US62 standard) and six aerosol types (continental, maritime, urban, desert, biomass burning, and haze). Haze is a user defined aerosol type, where the fraction of four aerosol particles–dust, water soluble, soot, and oceanic–is 15%, 75%, 10%, and 0%. The amount of water vapor is set to the default value, and the AOD at 550 nm is set to 0.1, 0.2, 0.25, 0.3, 0.35, and 0.4, which corresponds to a range from clear to relatively turbid aerosol loading conditions. The target altitude (land-surface elevation) varies from 0 to 3.5 km in increments of 0.5 km; the SZA varies from 0° to 80°, and

the VZA varies from 0° to 64°, both in 4° increments. The RAA varies from 0° to 180° in increments of 20°.

*C. Angular Bin Regression Analysis*

We used an angular bin regression approach to link the TOA directional reflectances to surface broadband albedos. To account for the anisotropy in TOA reflectance, the space of solar/view-geometry is divided into 3-D grids according to the ranges of solar zenith, view zenith, and relative azimuth. Each grid is referred to as an angular bin. Regression coefficients between broadband albedo and directional TOA reflectance are derived at each angular bin. As the size of the bin decreases, the RMSE of the fitting result decreases. Finally, the size of $4° \times 4° \times 20°$ is chosen for this paper, and the fitting results are good over most of the angular bins. The central angle of the SZA varies from 0° to 80°, in 4° increments (the solar zenith angular bins are 0°–2°, 2°–6°, ..., 78°–82°). The central angle of the VZA varies from 0° to 64°, in 4° increments (the view zenith angular bins are 0°–2°, 2°–6°, ..., 62°–66°); the central angle of the RAA varies from 0° to 180° in 20° increments (the relative azimuth angular bins are — 10°–10°, 10°–30°, ..., 170°–190°). In each angular bin, the TOA directional reflectances at different atmospheric conditions are simulated according to (9), and the kernel coefficients inverted by the POLDER-3/PARASOL BRDF are used to estimate the land-surface broadband albedos and the parameters used in (9).

Because the BRDF characteristics of different land surfaces are different, the data of the POLDER-3 BRDF database need to be classified before the regression analysis. We do not want to use a complex classification system such as IGBP or GLC2000, because they are not based on instantaneous state of the surface. For example, when grassland is covered with seasonal snow, its state is still grassland in the IGBP or GLC2000 systems, so the albedo change cannot be reflected. Instead, we classified the data set of only three major classes are considered: vegetation, soil, and snow/ice. However, to make a smooth transition between the major classes, we adopted the following strategy when building the training data sets. Initially, we divided the data sets into five parts: pure vegetation, pure bare soil, pure snow/ice, intermediate class A,

TABLE IV

CLASSIFICATION CRITERIA FOR THE POLDER BRDF DATABASE

| Criterions | Class | Samples |
|---|---|---|
| $0.22 < NDVI < 1$ | Pure vegetation | 4637 |
| $-1 < NDVI < 0.15$ and $0 < r_{490} < 0.25$ | Pure soil | 2401 |
| $r_{490} > 0.4$ | Pure snow/ice | 627 |
| $0.15 < NDVI < 0.22$ | Intermediate class A | 1136 |
| $0.25 < r_{490} < 0.4$ | Intermediate class B | 123 |

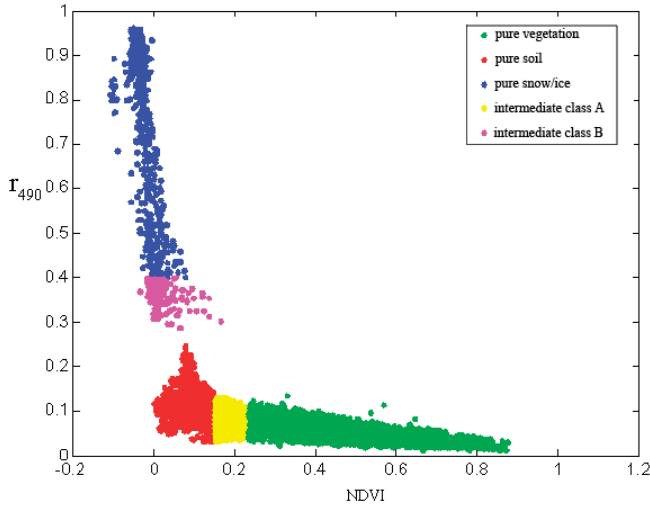$NDVI$ is an abbreviation for normalized difference vegetation index, and $r_{490}$ is the directional reflectance at wavelength of 490 nm



Fig. 2. Classification for POLDER-3/PARASOL BRDF database.

and intermediate class B (the classification criteria are shown in Table IV and Fig. 2). Then we merged them into three classes: vegetation (pure vegetation + intermediate class A), soil (pure soil + intermediate class A + intermediate class B), and snow/ice (pure snow/ice + intermediate class B). In the angular bin regression procedure, the data sets of different classes are analyzed separately.

The relationship between TOA directional reflectances and broadband albedos can be expressed by

$$\alpha_{ws} = m_0 + \sum_{i=1}^{n} m_i \rho_i(\theta_s, \theta_v, \varphi) \qquad (10)$$

$$\alpha_{bs}(\theta_s(k)) = n_0(k) + \sum_{i=1}^{n} n_i(k)\rho_i(\theta_s, \theta_v, \varphi) \qquad (11)$$

where $\alpha_{ws}$ is the broadband white-sky albedo; $\alpha_{bs}(\theta_s(k))$ is the broadband black-sky albedo; $\theta_s(k)$ is the SZA, which varies from $0°$ to $80°$ in increments of $5°$; $\theta_s(k) = 0, 5, \ldots, 75, 80$; $k = 1, 2, 3, \ldots, 16, 17$; $i = 1, 2, 3$, and 4, representing the MODIS bands 648, 859, 466, and 544 nm, respectively; $m_0$ and $n_0(k)$ are the intersection terms of the regression equation, $m_i$ and $n_i(k)$ are the coefficients of the regression equation, the intersection terms and coefficients are used for different angular bins and land-cover classes. $\rho_i(\theta_s, \theta_v, \varphi)$ is the TOA directional reflectance derived from $\rho_i^{\text{TOA}}(\theta_s, \theta_v, \varphi)$, and $\rho_i(\theta_s, \theta_v, \varphi)$ is derived from the TOA directional reflectance by eliminating the water vapor absorption

$$\rho_i(\theta_s, \theta_v, \varphi) = \rho_i^{\text{TOA}}(\theta_s, \theta_v, \varphi)/t_{\text{H}_2\text{O}} \qquad (12)$$

where $\rho_i^{\text{TOA}}(\theta_s, \theta_v, \varphi)$ is the TOA reflectance, and $t_{\text{H}_2\text{O}}$ is the atmospheric water vapor transmittance in both the upward and downward directions.

### III. RESULTS

#### A. Analysis Based on the Simulated Data set

We examined the accuracy dependencies of the angular bin regression method for different angular bins, aerosol conditions, and land-cover types. For simplicity, the broadband albedos calculated by integrating the estimated results of the revised linear kernel-driven model are referred to as "reference albedo," and the broadband albedos calculated by the angular bin regression model are referred to as "estimated albedo." Two statistical parameters $R^2$ (coefficient of determination) and RMSE are selected to evaluate the robustness of the angular bin regression method.

*1) Accuracy Dependencies on Different Bin Sizes and Solar/View Angles:* Because the directional reflectance properties of land surfaces and the atmospheric parameters varies with the solar/view angles, the fitting results of different sizes of angular bins are different. Fig. 3 shows the average fitting RMSE with different bin sizes of VZA ($4°$ to $64°$ with $4°$ incensement) at three different SZAs [SZA = $20°$, $40°$, and $60°$; RAA = $100°$]. In all of the three SZAs, fitting RMSE decreases along with the bin size of VZA, indicating that the angular bin method is more accurate with smaller bins. On the other hand, smaller bin size means more computational resources. So, a compromise is inevitable. In general, $4°$ to $10°$ is adequate bin size for VZA and SZA to get reasonably good regression result. And the adequate bin size of RAA can be much larger than that of SZA and VZA ($\sim 20°$ to $60°$).

Although the direct-estimation algorithm can make adjustment for the surface anisotropy effect through angular bin division, the sun/view geometry still has an influence on the accuracy of the retrieved broadband albedo. The dependencies of this method on different solar/view angles are examined based on the simulated TOA BRDF data set, where there are 277 104 samples (5773 BRDF samples × 48 atmospheric conditions) in each angular bin; the land-cover type is vegetation; and the aerosol type is continental. In the principle plane, among 357 angular bins at 21 SZAs and 17 VZAs, the $R^2$ values for 303 angular bins (84.9%) are larger than 0.9, and the RMSE values for 312 angular bins (87.4%) are < 0.01. The fitting results show that the angular bin regression model has a strong ability to fit the data set of different angular bins.

The distribution of fitting $R^2$ in the view angle hemisphere is shown in Fig. 4, with SZA at $20°$, $40°$, and $60°$. At the different SZAs ($20°$, $40°$, and $60°$), the distribution patterns of fitting $R^2$ are similar. At the angles near the backward

This article has been accepted for inclusion in a future issue of this journal. Content is final as presented, with the exception of pagination.

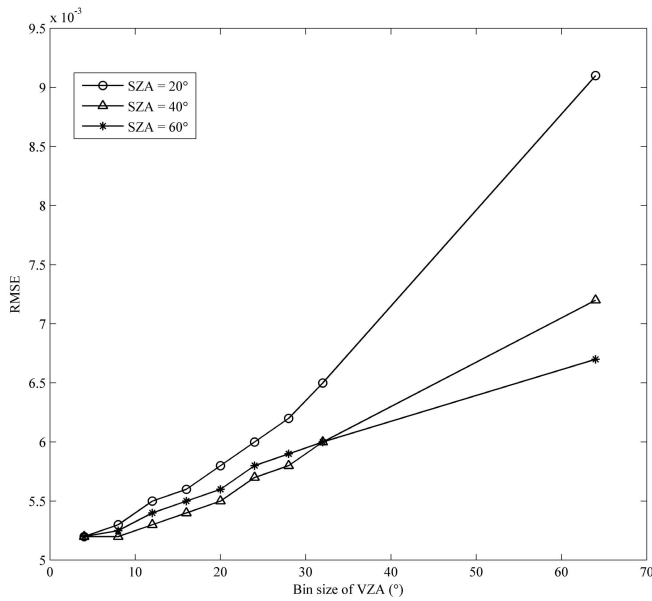QU *et al.*: DIRECT-ESTIMATION ALGORITHM FOR MAPPING DAILY LAND-SURFACE BROADBAND ALBEDO 7



Fig. 3. Fitting RMSE with different bin size of VZA (SZA = 20°, 40°, and 60°; RAA = 100°). Land-cover type: vegetation. Aerosol type: continental.



Fig. 4. Distribution of fitting R2 in the view angle hemisphere (a) SZA = 20°. (b) SZA = 40°. (c) SZA = 60°. Land-cover type: vegetation. Aerosol type: continental.

direction of the principal plane (RAA = 0°), $R^2$ increases as the VZA increases. At the angles near the forward direction of the principal plane (RAA = 180°), $R^2$ decreases as the VZA increases. The smallest $R^2$ occurs at the hot spot (RAA = 0°; when SZA = 20°, 40°, and 60°, VZA = 20°, 40°, and 60°), and the largest $R^2$ occurs at the larger VZA at perpendicular to the principal plane (RAA = 90°). In most cases, the angular bin regression method yields good results for different solar/view angles.

*2) Accuracy Dependencies on Different Aerosol Conditions:* The dependencies of the angular bin method on different aerosol types (continental, maritime, urban, desert, biomass burning, and haze) are examined. Fig. 5 shows the scatter plot of reference albedo and estimated albedo at six different aerosol types. The fitting result is good except the aerosol type of urban. When the aerosol type is urban, the estimation accuracy is seriously affected by the aerosol loadings, especially when the broadband albedo of land surfaces is > 0.5. For the other aerosol types, the estimation accuracy has no significant difference.

Fig. 6 shows the scatter plot of reference albedo and estimated albedo at different aerosol loadings (AOD = 0.10, 0.20, 0.30, and 0.40). The simulation results show that the angular bin regression method has little dependency on aerosol loadings when the aerosol type is continental. The capability of the angular bin regression method is similar to that of atmospheric correction using the full 6S atmospheric radiative transfer code. The albedos estimated using the angular bin regression model are quite consistent with the albedos calculated by integrating the revised linear kernel-driven coefficients, and most of the points cluster around the diagonal.

*3) Accuracy Dependencies on Different Land-Cover Types:* In Section II-C, the land observations are classified into vegetation, soil, and snow according to their spectral difference. The fitting results of different land-cover types of one of the angular bin are shown in Fig. 7. For this angular bin, the
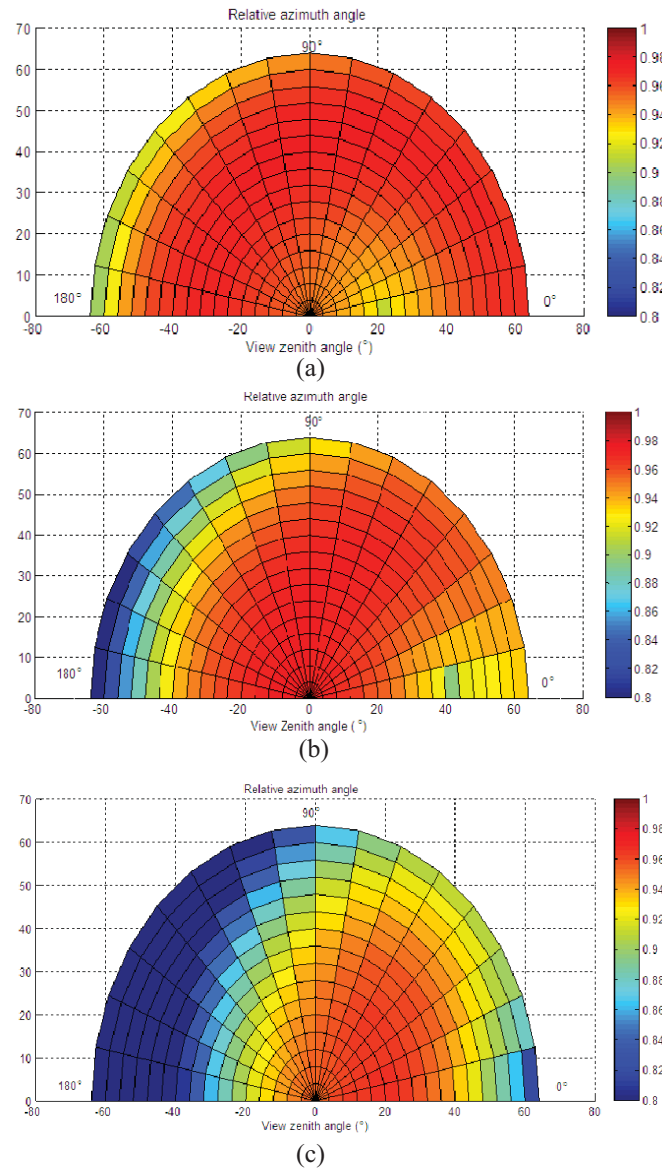
central SZA is 32°, the VZA is 0°, and the RAA is 180°, with RMSE of 0.012 for vegetation, 0.013 for soil, and 0.025 for snow/ice, respectively.

In conclusion, the angular bin regression model is very robust, and its accuracy depends on the angular bins, aerosol conditions, and land-cover types.

### B. Validation

The field-observed local noon albedos (ground-truth data) provided by FLUXNET are used to validate the broadband albedos estimated by the direct-estimation algorithm. In this paper, the land-surface broadband albedos at local noon are estimated using (10) and (11), whereas the coefficients of the angular bin regression model are precalculated and saved in a LUT. When the MODIS daily TOA reflectance product (MOD02) is acquired, the land-surface broadband albedos are estimated using the coefficients

This article has been accepted for inclusion in a future issue of this journal. Content is final as presented, with the exception of pagination.

8                                                                                                    IEEE TRANSACTIONS ON GEOSCIENCE AND REMOTE SENSING
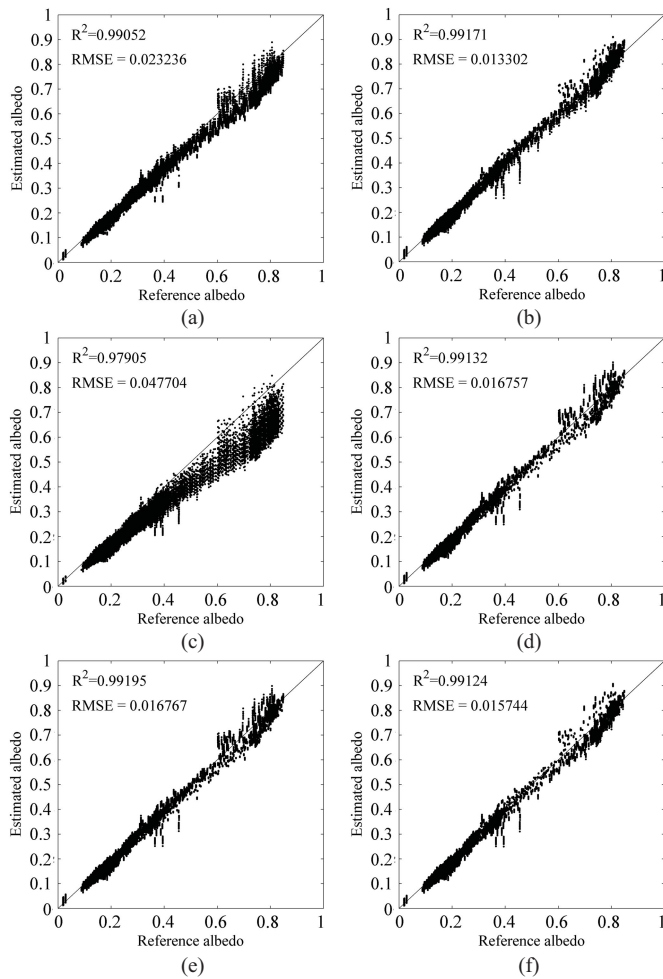


Fig. 5.   Scatter plot of reference albedo versus estimated albedo of different aerosol types. (a) Continental. (b) Maritime. (c) Urban. (d) Desert. (e) Biomass burning. (f) Haze.
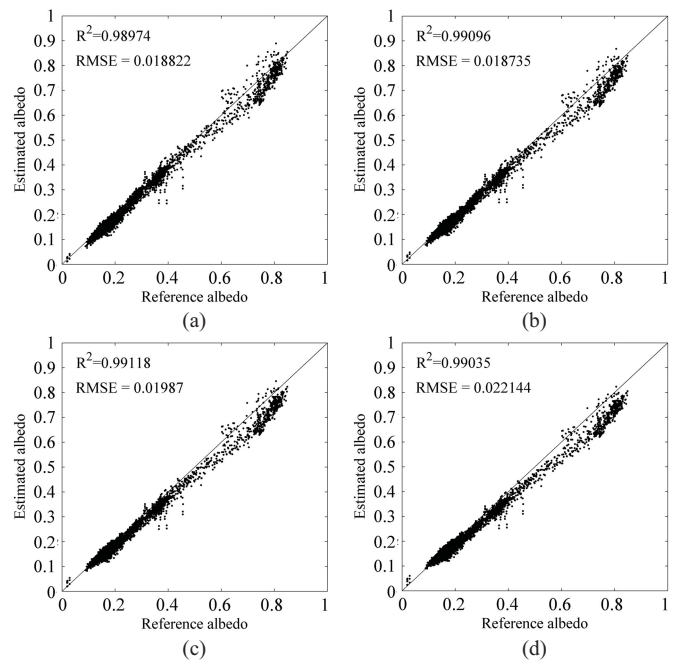


Fig. 6.   Scatter plot of reference albedo versus estimated albedo of different AOD. (a) AOD = 0.1. (b) AOD = 0.2. (c) AOD = 0.3. (d) AOD = 0.4. Aerosol type: continental.
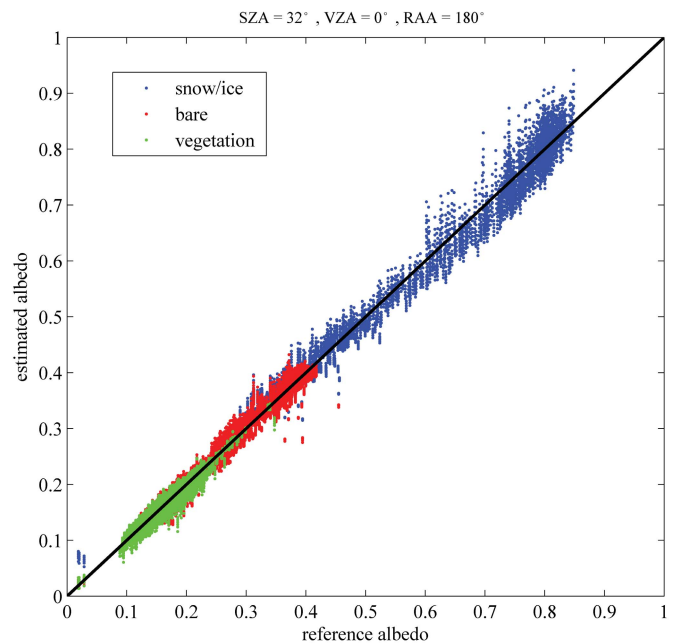


Fig. 7.   Scatter plot of reference albedo versus estimated albedo of different land-cover classes. Green points: are vegetation. Red points: soil. Blue points: snow or ice. Aerosol type: continental.

of different angular bins searched from the LUT. Field-observed albedo measurements are acquired from FLUXNET website (http://daac.ornl.gov/FLUXNET/fluxnet.shtml), which provides continuous observations of the exchanges of carbon dioxide, water vapor, and energy between the biosphere and the atmosphere. The long-term field measurements of upwelling/downwelling radiation flux are collected by the tower-mounted pyranometers at a series of sites. In [41], the spatial representativeness of FLUXNET sites is investigated, and 53 sites are considered to meet the criterion of homogeneity. Based on their study, the same 53 tower-based field measurement sites (shown in Table V) with ten different land-cover types are selected to validate the direct-estimation algorithm.

The time series of remote sensing retrieved daily albedo by direct-estimation algorithm in several typical FLUXNET sites are shown in Fig. 8, together with the ground measurements and the eight day MCD43B3 products. When doing the comparison, the blue-sky albedo is calculated by (5), where the fraction of skylight is calculated by a predetermined LUT based on 6S atmospheric radiative transfer code.

The land-cover type of the AU Tum site (35.66 °S, 148.15 °E) is evergreen broadleaf forests. From January 2002 to December 2004, the surface broadband albedo is ~0.1 in summer, and when snow falls in winter, the albedo increases dramatically to 0.25; when the snow melts in spring, the albedo decreases immediately. Fig. 8(a) shows that the direct-estimated albedos are consistent with the field-observed data.

The land-cover type of the US Fpe site (48.31 °N, 105.10 °E) is grasslands. From June 2002 to November 2005, the albedo increases dramatically from 0.15 to 0.8 when snow falls, and decreases immediately when the snow melts [Fig. 8(b)]. In the winter of November 2003 to April 2004, the direct-estimation algorithm obtained more estimation results

This article has been accepted for inclusion in a future issue of this journal. Content is final as presented, with the exception of pagination.

QU *et al.*: DIRECT-ESTIMATION ALGORITHM FOR MAPPING DAILY LAND-SURFACE BROADBAND ALBEDO 9

TABLE V

FIELD MEASUREMENTS ACQUIRED FROM FLUXNET

| N | Site ID | Country | IGBP Type | Latitude (degree) | Longitude (degree) | $ST_{score}$ leaf-on | $ST_{score}$ leaf-off |
|---|---|---|---|---|---|---|---|
| 1 | AU Tum | Australia | EBF | −35.66 | 148.15 | 9.75 | |
| 2 | AU Wac | Australia | EBF | −37.43 | 145.19 | 11.3 | |
| 3 | BR Cax | Brazil | EBF | −1.72 | −51.46 | 5.33 | |
| 4 | BR Sa3 | Brazil | EBF | −3.02 | −54.97 | 6.23 | |
| 5 | BW Ghg | Botswana | SAV | −21.51 | 21.74 | 0.67 | 0.6 |
| 6 | BW Ghm | Botswana | WSA | −21.2 | 21.75 | | |
| 7 | BW Ma1 | Botswana | WSA | −19.92 | 23.56 | 5.42 | 3.4 |
| 8 | CA Ca1 | Canada | ENF | 49.87 | −125.33 | 5.99 | |
| 9 | CA Ca3 | Canada | ENF | 49.53 | −124.9 | 0.64 | |
| 10 | CA NS6 | Canada | OSH | 55.92 | −98.96 | | |
| 11 | CA SF2 | Canada | ENF | 54.25 | −105.88 | 1.72 | |
| 12 | CA SF3 | Canada | ENF | 54.09 | −106.01 | 3.14 | |
| 13 | CA WP1 | Canada | MF | 54.95 | −112.47 | 1.65 | 1.15 |
| 14 | CZ BK1 | Czech Republic | ENF | 49.5 | 18.54 | 3.18 | |
| 15 | DE Geb | Germany | CRO | 51.1 | 10.91 | 0.9 | 0.88 |
| 16 | DE Hai | Germany | DBF | 51.08 | 10.45 | 1.97 | 4.01 |
| 17 | DE Kli | Germany | CRO | 50.89 | 13.52 | 0.62 | 0.88 |
| 18 | DE Tha | Germany | ENF | 50.96 | 13.57 | 5.99 | |
| 19 | DE Wet | Germany | ENF | 50.45 | 11.46 | 1.55 | |
| 20 | ES ES2 | Spain | CRO | 39.28 | −0.32 | 0.91 | 1.04 |
| 21 | ES LMa | Spain | SAV | 39.94 | −5.77 | 1.89 | 1.89 |
| 22 | FR Fon | France | DBF | 48.48 | 2.78 | 0.51 | 0.64 |
| 23 | FR Hes | France | DBF | 48.67 | 7.07 | 1.44 | 1.21 |
| 24 | FR Pue | France | EBF | 43.74 | 3.6 | 0.87 | |
| 25 | GF Guy | French Guyana | EBF | 5.28 | −52.93 | 1.92 | |
| 26 | HU Bug | Hungary | GRA | 46.69 | 19.6 | 1.74 | 0.93 |
| 27 | IE Dri | Ireland | GRA | 51.99 | −8.75 | 1.05 | |
| 28 | IT Bon | Italy | ENF | 39.48 | 16.54 | 2.43 | |
| 29 | IT Col | Italy | DBF | 41.85 | 13.59 | 2.6 | 0.71 |
| 30 | IT SRo | Italy | ENF | 43.73 | 10.28 | 3.1 | |
| 31 | JP Mas | Japan | CRO | 36.05 | 140.03 | 1.15 | 1.2 |
| 32 | KR Kw1 | Korea | MF | 37.75 | 127.16 | 3.81 | 13.41 |
| 33 | NL Ca1 | Netherlands | GRA | 51.97 | 4.93 | 1.03 | 0.95 |
| 34 | NL Lan | Netherlands | CRO | 51.95 | 4.9 | 1.44 | 1.41 |
| 35 | NL Loo | Netherlands | ENF | 52.17 | 5.74 | 1.4 | |
| 36 | PT Esp | Portugal | EBF | 38.64 | −8.6 | 0.86 | |
| 37 | RU Che | Russia | MF | 68.61 | 161.34 | 0.54 | 0.44 |
| 38 | SE Nor | Sweden | ENF | 60.09 | 17.48 | 3.84 | |
| 39 | UK Gri | UK | ENF | 56.61 | −3.8 | 1.48 | |
| 40 | US Aud | USA | GRA | 31.59 | −110.51 | 0.62 | 1.12 |
| 41 | US Bn1 | USA | ENF | 63.92 | −145.38 | 0.56 | |
| 42 | US Bo1 | USA | CRO | 40.01 | −88.29 | | 1.48 |
| 43 | US Bo2 | USA | CRO | 40.01 | −88.29 | | 1.58 |
| 44 | US Fmf | USA | ENF | 35.14 | −111.73 | 3.08 | |
| 45 | US FPe | USA | GRA | 48.31 | −105.1 | 1.05 | 0.93 |
| 46 | US Fuf | USA | ENF | 35.09 | −111.76 | 1.72 | |
| 47 | US IB1 | USA | CRO | 41.86 | −88.22 | 0.76 | 0.77 |
| 48 | US Ivo | USA | WET | 68.49 | −155.75 | | |
| 49 | US MMS | USA | DBF | 39.32 | −86.41 | 8.75 | 6.87 |
| 50 | US MOz | USA | DBF | 38.74 | −92.2 | 2.17 | 3.17 |
| 51 | US SRM | USA | WSA | 31.82 | −110.87 | 2.13 | 1.48 |
| 52 | US WCr | USA | DBF | 45.81 | −90.08 | 1.82 | 2.94 |
| 53 | ZA Kru | South Africa | SAV | −25.02 | 31.5 | 1.34 | 1.28 |

Vegetation is coded according to the IGBP classification. EBF: evergreen broadleaf forests. SAV: savannas. WSA: woody savannas. ENF: evergreen needleleaf forests. OSH: open shrublands. MF: mixed forests. CRO: croplands. DBF: deciduous broad-leaf forests. GRA: grasslands. WET: Wetlands. $ST_{score}$ leaf-on and $ST_{score}$ leaf-off are indices of landscape heterogeneity derived from high-resolution scenes (enhanced thematic mapper plus) during the leaf-on and leaf-off seasons, respectively.

than did the traditional multiple-date-based algorithm during the snow fall and melt processes.

The land-cover type of FR Pue site (43.74 °N, 3.6 °E) is evergreen broadleaf forests. In 2006, as no snow falls in winter, the seasonal average of surface broadband albedo is ∼0.1, and this does not significantly change throughout the year. The albedos estimated by the direct-estimation algorithm are consistent with field-observations [Fig. 8(c)].

The land-cover type of the US Bo1 site (40.01 °N, 88.29 °W) is croplands. From May 2004 to December 2006, the surface broadband albedo changes drastically, with albedo changing from 0.1 to 0.25 during summer, and from 0.15 to 0.7 during winter [Fig. 8(d)]. The rise and fall of ground-truth albedos trends can be captured by the direct-estimation algorithm very well.

The land-cover type of CA NS6 site (55.92 °N, 98.96 °W) is open shrublands. The seasonal variations of this site from

This article has been accepted for inclusion in a future issue of this journal. Content is final as presented, with the exception of pagination.

10                                                                                                                    IEEE TRANSACTIONS ON GEOSCIENCE AND REMOTE SENSING
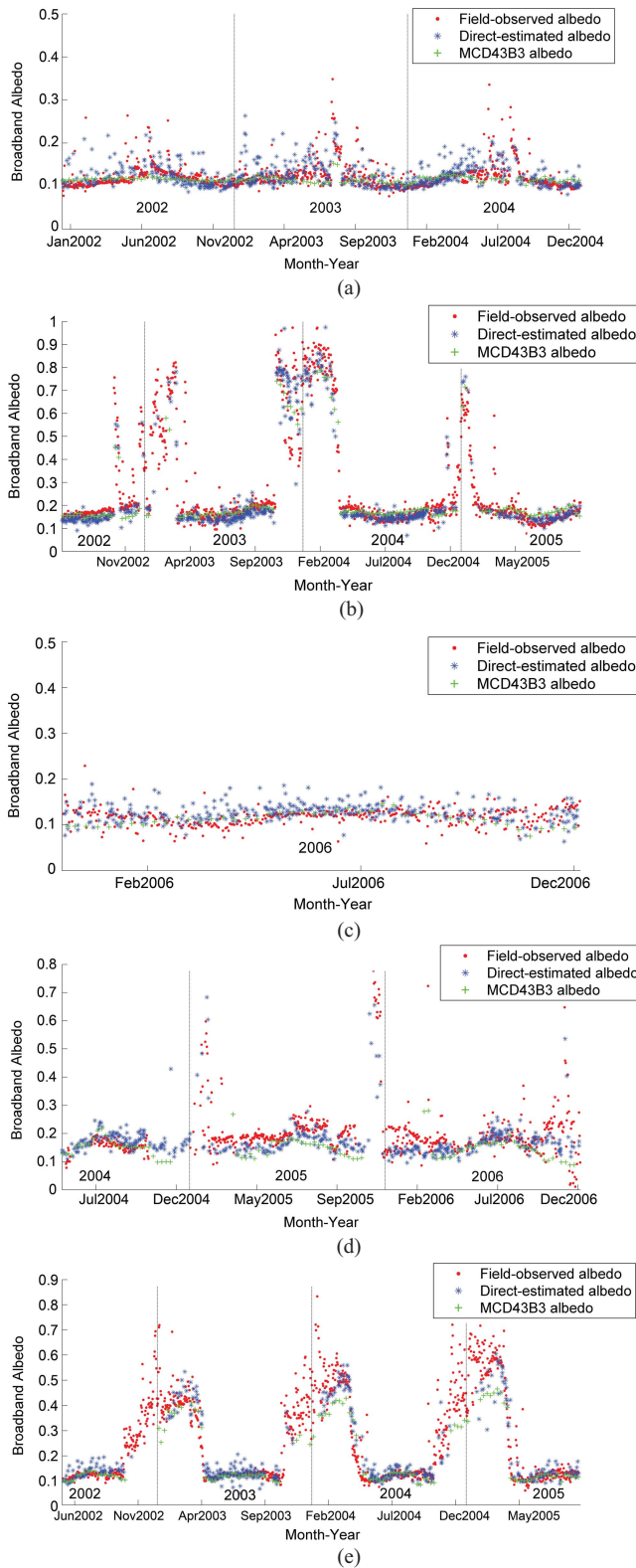


Fig. 8. Time series plots of surface broadband albedos estimated by the direct-estimation algorithm and field-observed ground data. (a) AU Tum, EBF, 2002–2004. (b) US Fpe, GRA, 2002–2006. (c) FR Pue, EBF, 2006. (d) US Bo1, CRO, 2004–2006. (e) CA NS6, OSH, 2002–2005. Red dots: field-observed albedos. Blue asterisks: albedos estimated by the direct-estimation algorithm. Green plus signs: albedos of the MCD43B3 product.



Fig. 9. Scatter plot of surface broadband albedo estimated by the direct-estimation algorithm and field-observed data, where 53 sites of (Table V) with ten different land-cover types are employed in this comparison. Ramp colors: number of scatters fall in each pixel ($0.008 \times 0.008$).
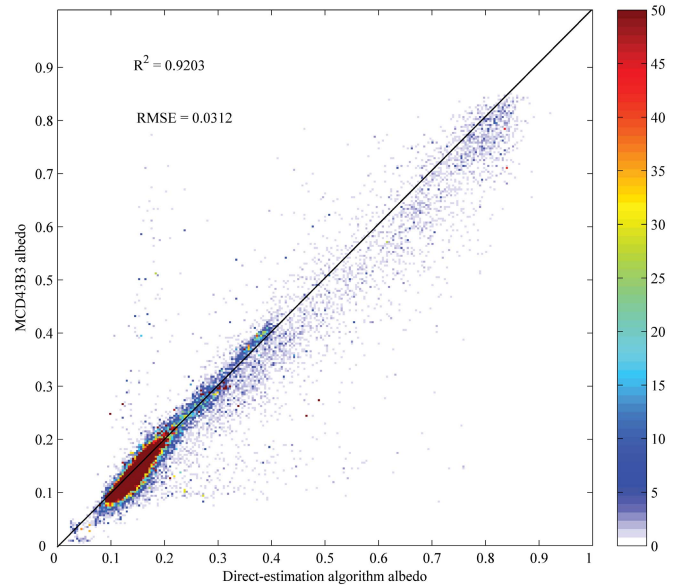


Fig. 10. Scatter plot of direct-estimation algorithm broadband black-sky albedo and MCD43B3 broadband black-sky albedo. Ramp colors: number of scatters fall in each pixel ($0.0035 \times 0.0035$).

May 2002 to September 2005 are shown in Fig. 8(e). The land-surface broadband albedo increases from 0.1 to ~0.15 in summer, and decreases in autumn. When snow falls, the albedo

gradually increases from 0.1 to ~0.6. Fig. 8(e) shows that the seasonal variation trends of albedo can be well captured by the direct-estimation algorithm, though the estimated albedos are a little higher than the field-observed albedos during summer at this site.

The scatter plots of estimated and ground observed daily albedo in all the 53 sites (Table V) are shown in Fig. 9, where the ramp color stands for the number of the scatter points that fall in each pixel. The overall $R^2$ is 0.8182, and RMSE is 0.0538. The quantitative assessment of this algorithm corresponds to the overall error of the direct-estimation algorithm.

The consistency of the direct-estimation algorithm and MCD43B3 product are also examined in this paper. We derived

This article has been accepted for inclusion in a future issue of this journal. Content is final as presented, with the exception of pagination.

QU *et al*.: DIRECT-ESTIMATION ALGORITHM FOR MAPPING DAILY LAND-SURFACE BROADBAND ALBEDO                                                                 11

an eight day albedo product by simply averaging the daily direct-estimated broadband albedo in a 16-day time window. One thousand seven hundred thirty-nine pixels around the world from 2006 to 2009 are selected for this comparison, including the sites that are usually used for *in situ* validation (FLUXNET sites, baseline Surface Radiation Network sites, thematically homogenous pixels selected by POLDER-3 BRDF database, and so on). The scatter plot of broadband black-sky albedo derived by direct-estimation algorithm and MCD43B3 product is shown in Fig. 10. The overall $R^2$ is 0.9203, and RMSE is 0.0312. The comparison result shows that the overall accuracy of the direct-estimation algorithm, which is derived without doing atmospheric corrections, is consistent with the current widely used MCD43B3 product.

## C. Discussion

The preliminary validation of the direct-estimation algorithm indicates reasonably good results. The retrieved albedos are in good agreement with the ones of MODIS product though they are derived from different algorithms. As a merit of the direct-estimation algorithm, it is capable of generating albedo product in daily temporal resolution, which will reflect the dynamic of land-surface albedo better than the traditional multiple-date-based algorithm. However, the direct-estimation algorithm is still sensitive to the clouds and other noise sources, and the preliminary results should be filtered based on the dynamic process models.

Based on the simulation results, the theoretical average uncertainty of the algorithm is ∼0.009 for vegetation, 0.012 for soil, and 0.030 for snow/ice. This uncertainty estimation is based on the assumption that surface BRDF and atmosphere radiative transfer are accurately modeled. Noise in satellite observations is also not considered in this analysis. So, much larger estimation errors should be expected when applying this method to real satellite data.

This algorithm involves three limitations that should be taken into consideration.

1) This algorithm constitutes an empirical model based on a training BRDF data set. As a result, the performance of the algorithm is limited by the representativeness of training data set, as well as the accuracy of surface BRDF and atmospheric radiative transfer model that is adopted in the simulation. In addition, because this algorithm only uses one scene of MODIS data for each estimation process, the algorithm may be more sensitive to noise than the multiobservation-based algorithm, especially when clouds and snow mix in the image pixels.
2) Although the POLDER-3/PARASOL BRDF database is the most suitable training data for this paper, the data set's resolution is much lower than that of the MODIS data. We readily admit that this is a probable source of uncertainty for this algorithm; the scale effects of the training data set need to be studied in the future.
3) In this paper, the broadband albedo estimated by the proposed method is preliminarily validated against ground-based point measurements. However, the spatial resolution of tower-observed albedos is not consistent with albedos estimated from satellite observations. Fur-

ther validations based on high-resolution satellite data for scaling-up [42] are still needed.

## IV. CONCLUSION

The temporal and spatial variation of land-surface broadband albedo was critical information for global change studies. A daily albedo product was needed, especially when the albedo changes rapidly, such as when snow was falling or melting. In this paper, a direct-estimation algorithm was proposed for estimating daily land-surface broadband albedo using MODIS data. This method builds a linear relationship between the TOA directional reflectances and land-surface broadband albedos using an angular bin regression method. Because the requirements for data and the associating data preprocessing were minimized, this method enables the production of daily broadband albedos. This paper has improved the algorithm in several ways.

1) An atmospheric radiative transfer simulation method was applied to replace the usual atmospheric correction procedure. In the previous paper, the atmospheric radiative transfer simulation method was based on the Lambertian assumption, whereas a fast, accurate analytical equation that accounts for BRDF effects was used in this paper.
2) The current standard MODIS BRDF/albedo algorithm needs 16-day composite atmospheric-corrected reflectance data to retrieve the land-surface albedo with a linear kernel-driven model, whereas only one scene of MODIS data is needed in our algorithm, so that daily albedo product can be generated. Validation results showed that the direct-estimation method is consistent with the current standard MODIS BRDF/albedo product and with improved capability for characterizing the temporal variation of albedo, especially when the land-surface BRDF changes rapidly.
3) The POLDER-3/PARASOL BRDF database was employed in this paper. The POLDER instrument provides much better angular sampling of the viewing direction hemisphere than MODIS [11]. The BRDF database served as a training data set that allows for a complete representation of the BRDF characteristics of land surfaces in global scope.
4) The proposed algorithm uses a precalculated LUT to estimate the land-surface broadband albedo, so it is efficient and suitable for producing long-term global albedo products [43].

This article has been accepted for inclusion in a future issue of this journal. Content is final as presented, with the exception of pagination.

12                                                                                                                    IEEE TRANSACTIONS ON GEOSCIENCE AND REMOTE SENSING

## References

[1] R. Dickinson, "Land processes in climate models," *Remote Sens. Environ.*, vol. 51, no. 1, pp. 27–38, Jan. 1995.

[2] S. Liang, *Quantitative Remote Sensing of Land Surfaces*. New York, USA: Wiley, 2004.

[3] S. Liang, K. Wang, X. Zhang, and M. Wild, "Review on estimation of land surface radiation and energy budgets from ground measurement, remote sensing and model simulations," *IEEE J. Special Topics Appl. Earth Observat. Remote Sens.*, vol. 3, no. 3, pp. 225–240, Sep. 2010.

[4] F. Gao, C. B. Schaaf, A. H. Strahler, A. Roesch, W. Lucht, and R. Dickinson, "MODIS bidirectional reflectance distribution function and albedo climate modeling grid products and the variability of albedo for major global vegetation types," *J. Graph. Res.*, vol. 110, pp. 1–13, Jan. 2005.

[5] W. Lucht, C. B. Schaaf, and A. H. Strahler, "An algorithm for the retrieval of albedo from space using semiempirical BRDF models," *IEEE Trans. Geosci. Remote Sens.*, vol. 38, no. 2, pp. 977–998, Mar. 2002.

[6] C. B. Schaaf, F. Gao, A. H. Strahler, W. Lucht, X. Li, T. Tsang, N. C. Strugnell, X. Zhang, Y. Jin, J.-P. Muller, P. Lewis, M. Barnsley, P. Hobson, M. Disney, G. Roberts, M. Dunderdale, C. Doll, R. P. D'Entremont, B. Hu, S. Liang, J. L. Privette, and D. Roy, "First operational BRDF, albedo nadir reflectance products from MODIS," *Remote Sens. Environ.*, vol. 83, nos. 1–2, pp. 135–148, Nov. 2002.

[7] C. Bacour and F.-M. Bréon, "Variability of biome reflectance directional signatures as seen by POLDER," *Remote Sens. Environ.*, vol. 98, no. 1, pp. 80–95, 2005.

[8] P. Bicheron and M. Leroy, "Bidirectional reflectance distribution function signatures of major biomes observed from space," *J. Graph. Res.*, vol. 105, no. D21, pp. 26669–26681, Jan. 2000.

[9] O. Hautecœur and M. M. Leroy, "Surface bidirectional reflectance distribution function observed at global scale by POLDER/ADEOS," *Geophys. Res. Lett.*, vol. 25, no. 22, pp. 4197–4200, Nov. 1998.

[10] M. Leroy, J. L. Deuzé, F. M. Bréon, O. Hautecoeur, M. Herman, J. C. Buriez, D. Tanré, S. Bouffiès, P. Chazette, and J. L. Roujean, "Retrieval of atmospheric properties and surface bidirectional reflectances over land from POLDER/ADEOS," *J. Geophys. Res.*, vol. 102, no. D14, pp. 17023–17037, Jan. 1997.

[11] F. Maignan, F. M. Bréon, and R. Lacaze, "Bidirectional reflectance of Earth targets: Evaluation of analytical models using a large set of spaceborne measurements with emphasis on the Hot Spot," *Remote Sens. Environ.*, vol. 90, no. 2, pp. 210–220, Mar. 2004.

[12] J. Muller. (2008, Dec. 1). *BRDF/Albedo Retrieval CA* [Online]. Available: http://www.brockmann-consult.de/albedomap/documentation.html

[13] D. Rutan, T. Charlock, F. Rose, S. Kato, S. Zentz, and L. Coleman, "Global surface albedo from CERES/TERRA surface and atmospheric radiation budget (SARB) data product," in *Proc. 12th Conf. Atmospheric Radiat.*, 2006, pp. 10–44.

[14] B. Geiger, J. Roujean, D. Carrer, and C. Meurey, "Product user manual (PUM) land surface albedo," Eumetsat, Germany Darmstadt, Germany, Tech. Rep. SAF/LAND/MF/PUM_Al/1.6v2, 2005.

[15] W. J. D. V. Leeuwen and J.-L. Roujean, "Land surface albedo from the synergistic use of polar (EPS) and geo-stationary (MSG) observing systems: An assessment of physical uncertainties," *Remote Sens. Environ.*, vol. 81, nos. 2–3, pp. 273–289, Aug. 2002.

[16] Y. M. Govaerts and A. Lattanzio, "Retrieval error estimation of surface albedo derived from geostationary large band satellite observations: Application to Meteosat-2 and Meteosat-7 data," *J. Geophys. Res.*, vol. 112, no. D5, p. D05102, Mar. 2007.

[17] Y. Govaerts, A. Lattanzio, M. Taberner, and B. Pinty, "Generating global surface albedo products from multiple geostationary satellites," *Remote Sens. Environ.*, vol. 112, no. 6, pp. 2804–2816, 2008.

[18] Y. M. Govaerts, B. Pinty, M. Taberner, and A. Lattanzio, "Spectral conversion of surface albedo derived from meteosat first generation observations," *IEEE Geosci. Remote Sens. Lett.*, vol. 3, no. 1, pp. 23–27, Jan. 2006.

[19] B. Pinty, F. Roveda, M. Verstraete, N. Gobron, Y. Govaerts, J. V. Martonchik, D. J. Diner, and R. A. Kahn, "Surface albedo retrieval from Meteosat 1. Theory," *J. Geophys. Res.*, vol. 105, no. D14, pp. 18099–18112, Jan. 2000.

[20] B. Pinty, F. Roveda, M. M. Verstraete, N. Gobron, Y. Govaerts, J. V. Martonchik, D. J. Diner, and R. A. Kahn, "Surface albedo retrieval from Meteosat 2. Applications," *J. Geophys. Res.*, vol. 105, no. D14, pp. 18113–18134, Jan. 2000.

[21] S. Liang, H. Fallah-Adl, S. Kalluri, J. JáJá, Y. Kaufman, and J. R. G. Townshend, "An operational atmospheric correction algorithm for landsat thematic mapper imagery over the land," *J. Geophys. Res.*, vol. 102, no. D14, pp. 17173–17186, Jan. 1997.

[22] C. Schaaf, Y. Shuai, Z. Wang, A. H. Strahler, X. Zhang, D. P. Roy, R. E. Wolfe, K. Strabala, and L. Gumley, "Monitoring albedo and vegetation phenology with the modis daily direct broadcast reflectance anisotropy algorithm," American Geophysical Union, Washington, DC, USA, Tech. Rep. IN33C-03, 2010.

[23] P. Mason, "Implementation plan for the global observing systems for climate in support of the UNFCCC," GCOS, Asheville, NC, USA, Tech. Rep. WMO/TD 1219, 2004.

[24] S. Liang, A. H. Strahler, and C. Walthall, "Retrieval of land surface albedo from satellite observations: A simulation study," *J. Appl. Meteorol.*, vol. 38, pp. 712–725, Aug. 1999.

[25] S. Liang, "A direct algorithm for estimating land surface broadband albedos from MODIS imagery," *IEEE Trans. Geosci. Remote Sens.*, vol. 41, no. 1, pp. 136–145, Jan. 2003.

[26] S. Liang, J. Stroeve, and J. E. Box, "Mapping daily snow/ice shortwave broadband albedo from Moderate Resolution Imaging Spectroradiometer (MODIS): The improved direct retrieval algorithm and validation with Greenland in situ measurement," *J. Geophys. Res.*, vol. 110, p. D10109, May 2005.

[27] Y. Cui, Y. Mitomi, and T. Takamura, "An empirical anisotropy correction model for estimating land surface albedo for radiation budget studies," *Remote Sen. Environ.*, vol. 113, no. 1, pp. 24–39, Jan. 2009.

[28] E. Vermote, D. Tanré, J. Deuzé, M. Herman, and J. Morcrette, "Second simulation of the satellite signal in the solar spectrum, 6S: An overview," *IEEE Trans. Geosci. Remote Sens.*, vol. 35, no. 3, pp. 675–686, May 1997.

[29] S. Liang, "Narrowband to broadband conversions of land surface albedo I: Algorithms," *Remote Sens. Environ.*, vol. 76, no. 2, pp. 213–238, Nov. 2001.

[30] Z. Wang, C. B. Schaaf, M. J. Chopping, A. H. Strahler, J. Wang, M. O. Román, A. V. Rocha, C. E. Woodcock, and Y. Shuai, "Evaluation of Moderate-Resolution Imaging Spectroradiometer (MODIS) snow albedo product (MCD43A) over tundra," *Remote Sens. Environ.*, vol. 117, pp. 264–280, Nov. 2011.

[31] W. Wanner, X. Li, and A. H. Strahler, "On the derivation of kernels for kernel-driven models of bidirectional reflectance," *J. Geophys. Res.*, vol. 100, no. D10, pp. 21077–21090, Oct. 1995.

[32] J. L. Roujean, M. Leroy, and P. Y. Deschamps, "A bidirectional reflectance model of the Earth's surface for the correction of remote sensing data," *J. Geophys. Res.*, vol. 97, no. D18, pp. 20455–20468, Dec. 1992.

[33] W. Abdalati and K. Steffen, "Snowmelt on the Greenland ice sheet as derived from passive microwave satellite data," *J. Climate*, vol. 10, no. 2, pp. 165–175, Feb. 1997.

[34] A. H. Strahler, J. P. Muller, W. Lucht, C. B. Schaaf, T. Tsang, F. Gao, X. Li, P. Lewis, and M. Barnsley, "MODIS BRDF/albedo product: Algorithm theoretical basis document version 5.0," *J. Arid Environ.*, vol. 74, no. 5, pp. 540–548, 1999.

[35] H. Rahman, B. Pinty, and M. M. Verstraete, "Coupled surface-atmosphere reflectance (CSAR) model 2. Semiempirical surface model usable with NOAA advanced very high resolution radiometer data," *J. Geophys. Res.*, vol. 98, no. D11, pp. 20791–20801, Jan. 1993.

This article has been accepted for inclusion in a future issue of this journal. Content is final as presented, with the exception of pagination.

QU *et al.*: DIRECT-ESTIMATION ALGORITHM FOR MAPPING DAILY LAND-SURFACE BROADBAND ALBEDO 13

[36] O. Samain, B. Geiger, and J. L. Roujean, "Spectral normalization and fusion of optical sensors for the retrieval of BRDF and albedo: Application to VEGETATION, MODIS, and MERIS data sets," *IEEE Trans. Geosci. Remote Sens.*, vol. 44, no. 11, pp. 3166–3179, Nov. 2006.

[37] S. Liang, C. Shuey, A. Russ, H. Fang, M. Chen, C. Walthall, C. Daughtry, and R. Hunt, "Narrowband to broadband conversions of land surface albedo: II. Validation," *Remote Sens. Environ.*, vol. 84, no. 1, pp. 25–41, 2003.

[38] M. O. Román, C. B. Schaaf, P. Lewis, F. Gao, G. P. Anderson, J. L. Privette, A. H. Strahler, C. E. Woodcock, and M. Barnsley, "Assessing the coupling between surface albedo derived from MODIS and the fraction of diffuse skylight over spatially-characterized landscapes," *Remote Sens. Environ.*, vol. 114, no. 4, pp. 738–760, 2010.

[39] J. Stroeve, J. Box, F. Gao, S. Liang, A. Nolin, and C. Schaaf, "Accuracy assessment of the MODIS 16-day albedo product for snow: Comparisons with Greenland in situ measurements," *Remote Sens. Environ.*, vol. 94, no. 1, pp. 46–60, 2005.

[40] W. Qin, J. Herman, and Z. Ahmad, "A fast, accurate algorithm to account for non-lambertian surface effects on TOA radiance," *J. Geophys. Res.*, vol. 106, no. D19, pp. 22671–22684, 2001.

[41] A. Cescatti, B. Marcolla, S. K. Santhana Vannan, J. Y. Pan, M. O. Román, X. Yang, P. Ciais, R. B. Cook, B. E. Law, and G. Matteucci, "Intercomparison of MODIS albedo retrievals and in situ measurements across the global FLUXNET network," *Remote Sens. Environ.*, vol. 121, pp. 323–334, Jun. 2012.

[42] S. Liang, H. Fang, M. Chen, C. Shuey, C. Walthall, C. Daughtry, J. Morisette, C. Schaaf, and A. Strahler, "Validating MODIS land surface reflectance and albedo products: Methods and preliminary results," *Remote Sens. Environ.*, vol. 83, nos. 1–2, pp. 149–162, Nov. 2002.

[43] S. Liang, X. Zhao, W. Yuan, S. Liu, X. Cheng, Z. Xiao, X. Zhang, Q. Liu, J. Cheng, H. Tang, Y. H. Qu, Y. Bai, Y. Qu, H. Ren, K. Yu, and J. Townshend, "A long-term global land surface satellite (GLASS) dataset for environmental studies," *Int. J. Digit. Earth*, 2013, to be published.

**Shunlin Liang** (M'94–SM'01–F'13) received the Ph.D. degree in remote sensing and GIS from Boston University, Boston, MA, USA.

He was a Post-Doctoral Research Associate with Boston University from 1992 to 1993, and a Validation Scientist with the NOAA/NASA Pathfinder AVHRR Land Project from 1993 to 1994. He is currently a Professor with the University of Maryland, College Park, MD, USA. His current research interests include spatio-temporal analysis of remotely sensed data, integration of data from different sources and numerical models, and linkage of remote sensing with global environmental changes. He has authored the book *Quantitative Remote Sensing of Land Surfaces* (Wiley, 2004) and edited the book *Advances in Land Remote Sensing: System, Modeling, Inversion and Application* (Springer, 2008). He is a member of NASA ASTER and MODIS science teams and NOAA GOES-R Land science team.

Dr. Liang is a Co-Chairman of the International Society for Photogrammetry and Remote Sensing Commission VII/I Working Group on Fundamental Physics and Modeling. He is an Associate Editor of the IEEE TRANSACTIONS ON GEOSCIENCE AND REMOTE SENSING, Subject Editor of the *Annals of GIS*, and also a Guest Editor of several remote sensing journals.
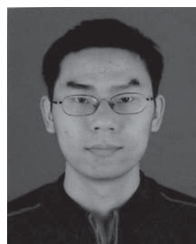
**Lizhao Wang** received the B.S. degree in GIS from Beijing Normal University, Beijing, China, in 2008. He is a graduate student at Beijing Normal University, Beijing.

His current research interests include albedo retrieving and validation methods.

**Ying Qu** received the B.S. degree in GIS from Beijing Normal University, Beijing, China, in 2008, where he is currently pursuing the Ph.D. degree.

His current research interests include retrieval of land surface biophysical parameters and BRDF/albedo from satellite data. His current research is mapping BRDF/albedo over snow/ice surfaces from multiple remote sensing data sources.

**Nanfeng Liu** received the B.S. degree in remote sensing science and technology from the Nanjing University of Information Science and Technology, Nanjing, China, in 2009. He is a graduate student with the Institute of Remote Sensing Applications, Chinese Academy of Sciences, Beijing, China.

His current research interests include gap-filling methods of albedo products and albedo retrieving methods.

**Qiang Liu** received the B.S. degree in computational mathematics from Beijing University, Beijing, China, in 1997, and the Ph.D. degree in cartography and remote sensing from the Institute of Remote Sensing Applications, Chinese Academy of Sciences, Beijing, in 2002.
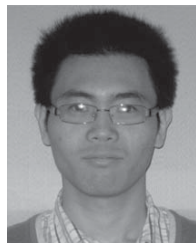
He is currently a Senior Scientist with the College of Global Change and Earth System Science, Beijing Normal University, and also with the State Key Laboratory of Remote Sensing Science, jointly sponsored by the Institute of Remote Sensing Applications of Chinese Academy of Sciences and Beijing Normal University. His current research interests include multi-angular remote sensing, such as geometric processing of multi-angular images, BRDF/albedo modeling and component temperature retrieval. His current research is to generate long time series of global BRDF/albedo from multiple remote sensing data sources.

**Suhong Liu** received the B.S. degree in computer science from Southwest Jiaotong University, Chengdu, China, in 1988, the M.Eng. degree in geophysical well-logging from Jianghan Petroleum University, Jingzhou, China, in 1991, and the Ph.D. degree in cartography and remote sensing from the Institute of Remote Sensing Applications, Chinese Academy of Sciences, Beijing, in 1999.

She is currently an Associate Professor with the School of Geography, Beijing Normal University, and also with the State Key Laboratory of Remote Sensing Science, jointly sponsored by the Institute of Remote Sensing Applications of Chinese Academy of Sciences and Beijing Normal University. Her current research interests include spatio-temporal analysis of remotely sensed data, retrieval of land surface biophysical parameters from satellite data, and geological remote sensing.